

AD-A045 386

NORTHWESTERN UNIV EVANSTON ILL DEPT OF MECHANICAL E--ETC F/G 20/2
A METAL CLUSTER GENERATOR FOR GAS PHASE ELECTRON DIFFRACTION AN--ETC(U)
SEP 77 A YOKOZEKI; O D STEIN

N00014-76-C-0378

UNCLASSIFIED

TR-3

NL

| OF |
AD
A045386



END
DATE
FILMED
11-77
DDC

ADA 045386

12
BS

September 1977

A METAL CLUSTER GENERATOR FOR GAS PHASE ELECTRON DIFFRACTION
AND ITS APPLICATION TO BISMUTH, LEAD AND INDIUM:
VARIATION IN MICROCRYSTAL STRUCTURE WITH SIZE

by

Michio Takasaki and Gilbert D. Spain

Distribution of this document is unlimited.

Report of Research for Contract N00014-75-C-0128;
Characterization of Metal and Metal Oxide Clusters Small Enough
to Determine the Critical Size for Gas Phase Polymerization in
Solution Systems (Power Branch, Office of Naval Research,
Arlington, VA). Submitted by Gilbert D. Spain, Principal
Investigator.

Reproduction in whole or in part is permitted for any purpose
of the United States Government.

PERMISSION TO REPRODUCE

UNRESTRICTED IN THE
PUBLIC DOMAIN
EXCEPT WHERE SHOWN
OTHERWISE

DDC
REF ID: A645386
SEP 1977

REPORT DOCUMENTATION PAGE		READ INSTRUCTIONS BEFORE COMPLETING FORM
1. REPORT NUMBER N00014-76-C-0378-TR3 ✓	2. GOVT ACCESSION NO.	3. RECIPIENT'S CATALOG NUMBER
6 4. TITLE (and Subtitle) A METAL CLUSTER GENERATOR FOR GAS PHASE ELECTRON DIFFRACTION AND ITS APPLICATION TO BISMUTH, LEAD AND INDIUM: VARIATION IN MICROCRYSTAL STRUCTURE WITH SIZE	5. TYPE OF REPORT & PERIOD COVERED ⑦ Technical Report	
	6. PERFORMING ORG. REPORT NUMBER ⑭ TR-3	
7. AUTHOR(s) ⑩ Akimichi/Yokozeki and Gilbert D./Stein	8. CONTRACT OR GRANT NUMBER(s) ⑮ N00014-76-C-0378 ✓	
9. PERFORMING ORGANIZATION NAME AND ADDRESS Northwestern University Dept. of Mechanical Engineering and Astronautical Sciences - Evanston, IL 60201 ✓	10. PROGRAM ELEMENT, PROJECT, TASK AREA & WORK UNIT NUMBERS NR092-544	
11. CONTROLLING OFFICE NAME AND ADDRESS Office of Naval Research Arlington, VA 22217	12. REPORT DATE ⑪ Sep 1977	
14. MONITORING AGENCY NAME & ADDRESS (if different from Controlling Office) ONR, Chicago 536 South Clark Street Chicago, IL 60605	13. NUMBER OF PAGES ⑫ 38 p.	
	18. SECURITY CLASS. (of this report) Unclassified	
16. DISTRIBUTION STATEMENT (of this Report) Distribution of this document is unlimited		
17. DISTRIBUTION STATEMENT (of the abstract entered in Block 20, if different from Report)		
18. SUPPLEMENTARY NOTES		
19. KEY WORDS (Continue on reverse side if necessary and identify by block number) Microcrystals, Clusters, Indium, Bismuth, Lead, Supersonic Free Jet, Nucleation, Electron Diffraction, Crystal Structure		
20. ABSTRACT (Continue on reverse side if necessary and identify by block number) An oven has been designed and built for the production of metal micro- crystals via nucleation and growth of the metal vapor in an inert gas atmosphere. It has a flowing argon, double orifice sampling system producing a supersonic free jet mixture which crosses a 40 kev electron beam. Debye- Scherrer diffraction patterns are obtained from the metal cluster samples which range in size from 40 to 95 Å in diameter with estimated concentrations		


403 502 JAB

of 10^{12} - 10^{13} cm^{-3} at the electron beam location. The average cluster size produced in the oven for all three metals studied correlated well with the product of oven pressure times metal evaporation temperature $p_0 T_{\text{om}}$. As $p_0 T_{\text{om}}$ increases, average size increases and cluster concentration decreases, in qualitative agreement with other metal evaporation research and with nucleation studies of vapor-inert gas expansions in supersonic nozzles. Analysis of the diffraction patterns reveal changes in crystal structure from that of the bulk in the neighborhood of 50-60 Å diameter (2,000 to 4,000 atoms per cluster). The differences are most pronounced in indium which changes from tetragonal to face centered cubic as the size decreases. Cluster temperatures at the electron beam location have been estimated from Debye-Waller factors, from extrapolation to bulk structure, and from calculated values of the argon gas temperature in the free jet. The three methods yield consistent results and the hotter the clusters are prior to the free jet expansion, the greater is the temperature difference between the clusters and the argon gas when the mixture becomes collisionless (i.e. no further change in the temperature of gas or clusters).

TABLE OF CONTENTS

	Page
ABSTRACT.	i
INTRODUCTION.	1
OVEN DESIGN	2
NUCLEATION AND GROWTH IN THE OVEN SOURCE.	3
SAMPLING THE ARGON-METAL CLUSTER MIXTURE: GASDYNAMICS.	8
CLUSTER COALESCENCE	10
ANALYSIS AND RESULTS.	11
Indium Clusters.	13
Lead Clusters.	14
Bismuth Clusters	15
DISCUSSION AND CONCLUSIONS.	15
ACKNOWLEDGEMENTS.	17
REFERENCES.	18
FIGURE CAPTIONS	20
TABLES.	22
FIGURES	27

ACCESSION for	
NTIS	Write Section <input checked="" type="checkbox"/>
DDC	Buff Section <input type="checkbox"/>
UNANNOUNCED	<input type="checkbox"/>
JUSTIFICATION _____	
BY _____	
DISTRIBUTION/AVAILABILITY CODES	
Dis. _____	SPECIAL _____
A	



INTRODUCTION

The objective of the work presented here is to determine the differences in structure of small metal microcrystals from that of the bulk phase as the average size is diminished. The size at which changes occur, as well as the nature of these changes, is of importance. The metal is vaporized in an oven in the presence of argon, an inert or "carrier" gas which initiates the metal nucleation and growth in the gas phase, near the evaporating surface. The newly formed microcrystals or clusters are entrained into a subsonic free jet and transported through a double orifice sampling arrangement. The portion of the argon-metal cluster mixture that passes through the second orifice or nozzle expands as a supersonic free jet and is crossed by a 40 kev electron beam 1 to 2 nozzle diameters downstream where diffraction patterns are taken on glass photographic plates.

The metal cluster source is designed to initiate the nucleation in the "stagnation" or pre-expansion chamber instead of the usual technique of expanding an unsaturated vapor through an orifice or nozzle. In the latter case the phase change occurs in the supersonic expansion. This choice was greatly influenced by the reported difficulty in getting metals to nucleate in adiabatic expansions. For example, mercury was reported as not clustering appreciably in nozzle beam-type expansions¹ and in large laval nozzles with cooling rates hundreds to thousands of times slower than those of the small free jets² (i.e. 10^5 °C/sec in contrast to 10^7 to 10^9 °C/sec in nozzle beams). One might predict such behavior, at least qualitatively, on the basis of the classical nucleation theory where the rate of formation of clusters large enough to initiate the condensed phase is given by³

$$J = K \exp(-\Delta G^*/kT) \quad . \quad (1)$$

Here J is the number of "critical" size clusters formed $\text{cm}^{-3} \text{sec}^{-1}$, k is Boltzmann's constant, T is temperature and K is a large pre-exponential factor dependent on the thermodynamic properties of the supersaturated state. The energy barrier for this Arrhenius-type rate equation is $\Delta G^* \sim \sigma^3 / T^2 \ln^2 S$, where σ is surface tension and the saturation ratio, $S = (p_v / p_\infty)_T$, is the ratio of the vapor pressure to the equilibrium vapor pressure at the same temperature. Because metals have surface tensions tens to hundreds of times higher than most gases, it requires enormous supersaturations to lower the energy barrier down to values encountered with gases. This can be accomplished by vaporization into an inert, cool gas atmosphere^{4,5}. This technique also greatly reduces the requirements of high oven power and large vacuum pumping capacity.

OVEN DESIGN

The oven cluster source of Fig. 1 represents a design evolution over several previous metal sources used in our laboratory in which the gas flow has been minimized. In addition, the necessary heater power is now low enough so that a highly regulated power supply can be used, requiring only minor adjustment of the electron beam with no jitter due to AC fields. This design also optimizes the cluster concentration at the crossed-beam intersection or scattering volume, providing several orders of magnitude increase over previous oven configurations.

The source is built to provide continuous $x - y$ motion during operation, relative to the electron beam. The x -motion for the oven as a unit is provided by the screws S_1 of Fig. 1. Between experiments the oven can be disassembled and the distance between orifices N_1 and N_2 changed by adjusting the screws S_2 shown also in Fig. 1. During an experiment the heater or metal source, argon supply jet, and the thermocouple can be continuously moved as a unit

relative to the orifices, or nozzles N_1 and N_2 . Varying this distance changes the flow time from the heater to the first nozzle N_1 . See Table I for dimensions and characteristic operating conditions.

The oven is operated with either a tungsten filament, or a boron nitride crucible with a coiled filament heater. Either configuration can be viewed using a window-prism arrangement. This is used to inspect the operation visually as well as providing access for an optical pyrometer. The argon supply and the pumping rate for the annular region between the orifices can be controlled so as to vary the pressure in the oven p_0 or, holding p_0 constant, to alter the jet velocity which controls the gas mixing time. The oven temperature is varied by adjustment of the filament power supply and measured with the optical pyrometer. The voltage drop across the filament and the amperage are recorded so that the power dissipated in the oven is known. The thermocouple which senses the gas temperature before it enters the first nozzle has a radiation shield over it to avoid direct radiant heating of the junction by the hot filament.

NUCLEATION AND GROWTH IN THE OVEN SOURCE

Most of the experiments reported here were conducted using a triple strand, coiled filament across the copper heater leads with the metal forming a spherical droplet of about 0.3 cm diameter near the center of the filament. A few experiments with lead were performed in a 0.5 cm diameter x 1 cm deep crucible. The nucleation and growth zone for the crucible is one-dimensional, while for the filament the zone is one-dimensional only if the zone location and thickness is small compared to 0.3 cm. Otherwise, it will be three-dimensional. If, in either configuration the flow in the nucleation zone is turbulent it would be most difficult to conceive a

meaningful theoretical model for the process. Turbulence alone without the complications of heat transfer, mass transport, and nucleation is difficult enough to describe theoretically. Estimates of the Reynolds number Re , for the argon flowing out of supply line near the heater, range from 10 to 50, which is well within the laminar flow regime (Recall $Re = \rho v l / \mu$ where ρ is gas density, v is velocity, l is a characteristic length and μ is the dynamic viscosity). Since the argon velocity over the filament or the crucible source is expected to be significantly lower than that at the argon supply, plus increased viscosity at the higher temperatures, the Reynolds number near the evaporating metal surface is even lower than the above values. There has been research to describe theoretically the nucleation in a laminar boundary layer⁶; and in no flow situations, i.e. stagnant films or layers^{7,8}; and diffusion cloud chambers^{9,10}. The case of the stagnant film nucleation has many features in common with adiabatic nozzle expansions⁸. If the oven produces convection whether natural¹¹ or forced¹², the flow geometry can become complicated, again making theoretical analysis difficult.

Due to the primary objective of this work, i.e. structure of small microcrystals formed in the gas phase, in addition to the above mentioned difficulties, a detailed description and analysis of the metal nucleation and growth process has not been undertaken. (Metal nucleation and growth for bismuth, lead, and iron has been studied in shock tube experiments¹³.) Certain gross features however are worth pointing out.

1) The increase in average size with oven temperature (or metal vapor density) reported by others^{5,14} has also been observed in this work. There is one interesting difference in the size determination however. Electron diffraction is used in the gas phase which probes the microcrystal size that

results from nucleation and growth only. Electron micrographs may or may not measure the primary microcrystal size in samples if coalescence of the microcrystals has occurred. Also, our argon pressure is a factor of 10 to 10^2 lower thus reducing the tendency for the microclusters to coalesce⁵.

2) The increase of cluster size with ambient argon pressure follows the trend observed in other evaporation studies⁵. This feature can be qualitatively explained since an increase in argon pressure inhibits the metal vapor mass transport shifting the nucleation and growth regions toward the higher vapor density region thus enhancing growth. This is similar to the explanation proposed to account for increased particle size with inert gas molecular weight (i.e. increased collision cross-section^{5,15}).

3) The results of items 1) and 2) above have been summarized in Fig. 2a. The variation of microcrystal "average" size with both the metal vapor temperature T_{om} (and therefore its pressure and density) and argon pressure p_o is plotted for the three metals investigated. This correlation is intended only as a qualitative indication since the actual process is governed by nucleation and growth requiring greater detailed knowledge of many more thermodynamic and flow properties than just p_o and T_{om} .

4) An estimate of cluster production rate and concentration at the electron beam location has been made. A few representative experiments for each metal are used, again only to indicate the approximate magnitude and trend of the cluster production. An upper limit estimate of the cluster flux or production rate is derived assuming that all the heater power is taken up by the heat of vaporization for the evaporating metal, neglecting losses due to radiation and to heat conduction to the argon. Dividing the resultant mass flux by the "average" cluster size obtained from the diffraction pattern

ring widths gives the cluster production rate \dot{N}_{cl} in clusters-sec⁻¹, which is shown in Fig. 2b.

Using the known spreading of the metal clusters in the supersonic free jet flow from N_2 (2.5° half angle), the location of the electron beam ($x_{eb}/D_{n2} \approx 1.5$), the terminal Mach number which occurs at or prior to $x/D_{n2} = 1.5$ ($M_T \approx 2.5$), and the cluster conservation relation $\dot{N}_{cl} = N_{cl}Av$ with A the jet cross-sectional area and v its velocity, the concentration N_{cl} at the scattering volume defined by the intersection of the free jet and the electron beam can be determined. If the cluster flux used is the maximum value then the cluster concentration will be the maximum or upper limit also. These calculated values of N_{cl} have been reduced by an order of magnitude as an estimate to account for: a) only a fraction of the electrical power is actually used for evaporation, b) some of the clusters will be transported to the walls of the oven source, and c) a fraction of the total argon-metal cluster mixture flow is pumped out of the annulus between N_1 and N_2 . Thus an estimated cluster concentration in the scattering or diffraction volume is obtained and is shown in Fig. 2b with the right-hand ordinate.

As with Fig. 2a these results are only qualitative. However, one obtains an estimate of concentration in the range of 10^{12} to 10^{13} clusters cm⁻³ and finds a decrease in N_{cl} with the product of oven pressure and oven temperature, $p_o T_{om}$, for all three metals. Thus a general picture of the nucleation and growth of metal clusters in the oven source emerges. The argon-metal vapor mixture cools rapidly with distance from the evaporating liquid metal surface. In spite of the decreasing vapor density with distance from the evaporating surface the metal vapor supersaturates increasingly with distance until it reaches a value high enough to cause a nucleation and growth process that is

rapid enough to deplete the vapor density and thus the supersaturation, shutting off the nucleation process. The remaining metal vapor condenses onto the clusters just formed. From the point where the nucleation rate approaches its maximum, the clusters formed may begin agglomeration or coalescence as well as growth by vapor deposition. From all indications, theoretical as well as experimental, the nucleation and growth zone or boundary layer is only a few tenths of a centimeter thick. As the metal surface temperature increases so does its local vapor pressure and density. The supersaturation profile moves in toward the surface causing the maximum nucleation zone to move with it. The higher density of the metal vapor here causes the clusters just nucleated to grow faster thereby shutting down the nucleation sooner. The net result then is a lower concentration of clusters and since there is more vapor present they grow to larger sizes. Thus, increasing the metal vapor pressure leads to the formation of fewer clusters of larger size.

Increasing the inert gas pressure (or inert gas collision cross-section, i.e. heavier molecular weight) enhances the heat transfer while inhibiting the mass transport. This also shifts the supersaturation curve in toward the evaporating surface with the same results as above, a smaller number of larger clusters formed. The structure of the nucleation and growth in a one-dimensional, stagnant film, thermal boundary layer has been treated by several authors^{7,8}. The similarities to condensation in supersonic, adiabatic nozzle flows are considerable⁸. The trends noted above are identical to those observed in moist air expansion in nozzles using pressure and light scattering measurements: i.e. increasing the condensable species partial pressure results in fewer clusters formed which then grow to larger sizes^{17,18}.

SAMPLING THE ARGON-METAL CLUSTER MIXTURE: GASDYNAMICS

The argon supply jet issues from a copper tube of 0.15 cm inside diameter which has been closed down at the end to 0.1 cm making a small converging section. The pressure at the inlet to the 15 cm long supply tube is typically 1.6 torr when $p_o = 1$ torr. Thus the pressure at the tube exit, though unknown, is close to the 1 torr value in the oven. The jet leaving the tube is thus subsonic and mixes with the ambient argon around the jet, setting into motion a convective flow in the remainder of the oven. In particular the metal vapor which nucleates and grows in a layer near the filament heater (or within the crucible as the case may be) is transported by this jet-induced circulation to the edge of the jet where it is entrained as the jet mixes with the convection flow. The mixture is pumped out through nozzle N_1 to a pressure of $p_1 = 0.6$ torr so the flow through N_1 is also subsonic. If it were isentropic then $p_1/p_o = 0.6/1$ gives a Mach number $M = 0.9$. Beyond the orifice N_1 the flow spreads out and some of it is pumped off with a mechanical vacuum pump of $140 \text{ liter min}^{-1}$ capacity. The mass flow to this pump can be varied with a valve. Then, in conjunction with a valve controlling the supply of argon at the inlet, the oven pressure p_o and total argon mass flow rate \dot{m}_a can be controlled independently. This provides control of p_o , an essential parameter for metal nucleation, as well as \dot{m}_a which determines the sampling or flow time from the heater to the nozzle N_1 . The intent then is to draw in the mixture using the mechanical pump and sample it with nozzle N_2 . Under the actual choice of operating conditions used, however, the greater fraction of the total mass flow goes through N_2 , i.e. typically 80% is seen in Table I. The pressure p_1 is not measured directly but inferred from the background pressure p_2 in the crossed beam chamber using an argon flow calibration previously made.

Using known mass flow rates and the appropriate dimensions, estimates of the gas velocities and flow times in the various chambers have been made. Note the different time scales: 15 to 400 milliseconds in the oven chamber, 10 to 100 microseconds in the intermediate pumping chamber, and 2 microseconds from N_2 to the electron beam.

The dimensionless ratio of viscous forces to dynamic forces is the Reynolds number Re and has been calculated for Table I at the inlet to the oven, and at nozzles N_1 and N_2 . Low values of Re are usually associated with laminar flow (e.g. in pipes $Re < 2000$). However even though the flow in the argon supply tube is laminar the free jet may be mixing turbulently downstream of the filament and in the conical region of the intermediate pumping chamber. The recirculation region in the oven chamber behind the argon supply jet as mentioned previously, is laminar with a Reynolds number much less than 20.

The ratio of the argon mean free path to a characteristic dimension is the Knudsen number, $Kn = \lambda/l$. It serves to delineate the regions of collision dominated or continuum flow, transition flow, and free molecular or collisionless flow by having values $\ll 1$, ≈ 1 , and $\gg 1$ respectively. Thus it is seen that the flow in the oven and through the nozzle N_1 is continuum while the supersonic flow through N_2 is approaching the transition regime. There are two important features which derive from the fact that the expansion through N_2 is approaching a Knudsen number of unity. One is that the x-position in the free jet at which the flow becomes collisionless is very close to the nozzle or free jet orifice¹⁶. The position at which collisions effectively terminate is $x/D_{n2} \approx 1^{12}$ or $x = 0.075$ cm with a typical value of terminal Mach number $M_T = 2.5$ and a terminal temperature $T_T = 117^\circ K$. Thus placing the electron beam any further downstream than $x/D_{n2} = 1$ will

not result in the measurement of any physical change in the clusters due to collisions, such as colder temperature or increased size. The only change with increasing x/D_{n2} is the undesirable trend to lower cluster concentration. The second feature of importance is that due to the relatively small number of collisions during the jet expansion, the jet does not spread out as much as a lower Knudsen number flow. The metal clusters spread through only a cone half angle of 2.5° as determined by collecting a metal film deposit at two different locations in the free jet, at $x = 0.15$ cm and $x \approx 50$ cm. This is important for good resolution of the Debye-Scherrer rings in the diffraction patterns. If the vertical extent of the free jet containing the metal clusters becomes an appreciable fraction of the camera length, i.e. the distance from the crossed beams to the film plane, the peaks would be additionally broadened in a manner difficult to deconvolute.

CLUSTER COALESCENCE

With cluster concentrations in the range of 10^{12} cm^{-3} as indicated by Fig. 2b, and characteristic times in the millisecond range or longer, coalescence is predicted theoretically¹⁸⁻²⁰ as well as experimentally observed^{12,21}. If coalescence occurs early in the nucleation and growth zone and the clusters are hot enough to still be liquid it is possible that they form larger homogeneous liquid droplets that later solidify⁵. The diffraction patterns from these microcrystals should be characteristic of the final droplet size. If on the other hand the clusters cool, solidify, and subsequently agglomerate they may adhere to one another due to local surface attractive forces and exhibit diffraction patterns characteristic of the primary microcrystals (i.e. those formed via nucleation and vapor growth only) as observed in polycrystalline thin films. Electron micrographs of coalesced particles may

under some circumstances reveal the primary cluster size and in other cases only show the final agglomerated size.

In all of the experiments conducted in this investigation, whether with lead, bismuth, or indium, in which cluster size is determined, there is a consistent relationship of average size with the properties which most directly affect the nucleation and growth zone, namely metal vapor temperature and argon pressure. On the other hand, a variation by a factor of two in sampling length from the heater to nozzle N_1 , causing a factor of two change in the longest characteristic flow time, produced no correlation with average cluster size. Although these correlations were not pursued in an extensive experimental program, and were of necessity qualitative due to the demands of our primary objectives, it is nevertheless tempting to conclude that coalescence did not significantly affect the structural features of the microclusters which are presented below.

ANALYSIS AND RESULTS

Diffraction patterns of In, Pb and Bi clusters are recorded on photographic plates (Kodak Electron Image - $3\frac{1}{2}$ x 4" plates) under the conditions described in the previous sections. Typical microdensitometer traces are illustrated in Fig. 3 (In and Pb) and Fig. 4 (Bi). Under the present experimental conditions, all diffraction patterns show relatively sharp Debye-Scherrer rings, i.e. no obvious liquid, molecular or small n-mer (dimer, trimer, etc.) patterns have been observed. The peak positions of diffraction patterns can be consistently assigned with the Miller indices (hkl) of the corresponding bulk crystals: In (D_{4h} - $I4/mmm$: body centered tetragonal), Pb (O_h^5 - $Fm\bar{3}m$: face centered cubic) and Bi (D_{3d}^5 - $R\bar{3}m$: hexagonal). In the case of In, however, diffraction patterns change their contour from the tetragonal to the f.c.c.

as the average size of cluster becomes small as illustrated in Fig. 3. Once the diffraction peaks are indexed, the values of the lattice parameter can be calculated from the following equations,

$$\text{In} : x/L\lambda = \left\{ 2(h^2 + k^2)/a^2 + l^2/c^2 \right\}^{\frac{1}{2}} \quad (2)$$

$$\text{Pb} : x/L\lambda = (h^2 + k^2 + l^2)^{\frac{1}{2}}/a \quad (3)$$

$$\text{Bi} : x/L\lambda = \left\{ 4(h^2 + k^2 + hk)/3a^2 + l^2/c^2 \right\}^{\frac{1}{2}} \quad (4)$$

$$x = r - 3r^2/8L^2 \quad , \quad (5)$$

where r is the radius of the Debye-Scherrer ring indexed as (hkl) , and $L\lambda$ is the camera constant determined by a standard thin metal film sample ($L = 53$ cm). The body centered tetragonal indium can be regarded as a distorted f.c.c. structure or f.c. tetragonal: $c/a \approx 1.075$ in a bulk crystal at room temperature.²² In Eqn. (2) for In, the lattice parameters (a and c) correspond to those in the distorted f.c.c., while for the f.c.c. indium patterns Eqn. (3) is applied. For Bi known as a rhombohedral structure, a hexagonal unit cell is used to determine the lattice parameters.

The average cluster size, D , is determined using the relation:

$$D = K\lambda/\beta \cos \theta \approx L\lambda/(W^2 - W_0^2)^{\frac{1}{2}} \quad (\theta \ll 1) \quad , \quad (6)$$

where λ is the electron wavelength, K is the shape factor ($K \approx 1.0$), θ is the Bragg angle, β is the true line broadening in radians, and W and W_0 are the half-widths of the lines of the sample and the reference (Au and Al standard thin films) materials, respectively. For the estimation of D , the well separated peaks have been used: (101) for In, (111) and (220) for Pb, and (102) for Bi.

The lattice parameters and average cluster diameter D are summarized in Tables 2,3 and 4, together with the corresponding experimental conditions. The lattice parameters and/or their ratio are plotted in Fig. 5 (In), Fig. 6 (Pb), and Fig. 7 (Bi) as functions of the cluster size (D) and the number of metal atoms per cluster (n).

Indium Clusters

A structure change mentioned earlier (Fig. 3) in In microcrystals can be more quantitatively observed in Fig. 5. The variation in lattice parameters a and c , and of their ratio, c/a , with cluster size, shows that a bulk f.c. tetragonal structure changes into f.c.c. structure near $D \approx 50 \text{ \AA}$ ($n \approx 3000$). This change involves a shrinkage in c and an expansion in the basal axis a , resulting in the unit cell volume remaining nearly constant ($\pm 0.1\%$). Another interesting aspect of this Figure is the essentially constant values in a and c , and thus also in the ratio c/a , beyond $D \approx 65 \text{ \AA}$ ($n \approx 5000$). This feature permits extrapolation of the lattice parameter data to large sizes and application of known bulk physical properties as one means of estimating cluster temperature. The thermal expansion coefficients of a bulk In crystal are known for a and c ²²:

$$\alpha_a = 25.4 \times 10^{-5} + 3.22 \times 10^{-10} T^2 \text{ and } \alpha_c = 23.0 \times 10^{-5} - 4.35 \times 10^{-10} T^2$$

($80^\circ\text{K} \leq T \leq 300^\circ\text{K}$). Using the extrapolated values of $a = 4.62 \text{ \AA}$ and $c = 4.89 \text{ \AA}$ and the above expansion coefficients, the cluster temperature T_{cl} is estimated to be $264 \pm 46^\circ\text{K}$. Similarly T_{cl} can be obtained from the extrapolation of c/a (1.058) and the unit cell volume (104.4 \AA^3): $T_{cl} = 362^\circ\text{K}$ and 294°K , respectively. A simple average of these three values is 307°K .

It is known that the lattice parameters of microcrystals decrease as the cluster size decreases^{23,24}. Such behavior for rare earth metals in thin film experiments has been interpreted in terms of surface tension and the bulk modulus²⁴. It should be noted, however, that the size dependence of c/a in the present result can not be explained by bulk compression due to the surface tension, since in bulk In crystals c/a increases monotonically with an increase in external pressure²⁵ (e.g. $c/a = 1.076$ at 0 kbar \rightarrow $c/a = 1.096$ at 151 kbar), while the present results show that c/a decreases as the cluster size decreases (i.e., as the pressure due to the surface tension increases).

In the present case the c/a ratio change of indium may arise from the stability of microcluster structure. For small clusters surface atoms represent a large fraction of the total number and crystal defects such as vacancies are more likely to occur in the surfaces of high curvature. These defects may play an important role with regard to cluster stability dictating a change from tetragonality to cubic indium.

Lead Clusters

The range of cluster sizes studied for Pb goes from $\sim 40 \text{ \AA}$ in diameter to $\sim 80 \text{ \AA}$, similar to the case for In. The results are shown in Table 3 and in Fig. 6. In contrast to In, the lattice parameters observed in this range of cluster size are essentially constant within an experimental error of $\sim 0.3\%$. The figure appears, however, to indicate a lattice parameter shrinkage below $D \leq 50 \text{ \AA}$ ($n \leq 2000$). An analysis of the Bragg peak intensities for the smallest clusters, $D \approx 40\text{-}50 \text{ \AA}$, shows a vestige of an amorphous solid; the detailed result will be published elsewhere. T_{cl} is estimated to be 212°K from the extrapolation of the lattice parameters, as has been made in In (see Fig. 6), using a linear thermal expansion coefficient of $\alpha = 27.08 \times 10^{-6} (\text{^\circ C})^{-1}$ ($90 \leq T \leq 287^\circ\text{K}$)²⁶. From a damping of Bragg peak intensities, i.e. Debye-Waller factor, T_{cl} for the largest cluster size has been estimated to be 150°K : $T_{cl} = (212 + 150)/2 = 181^\circ\text{K}$.

For the lead experiments two different types of oven sources are used to evaporate the metal; one is a tungsten wire coil similar to those used for In and Bi, and the other is a boron nitride crucible. The open circles in Fig. 6 correspond to data taken with the crucible oven, where the cluster sizes are relatively small, and show little variation in size with a change in $p_o T_{om}$. Although no systematic study of nucleation kinetics has been carried out, it certainly indicates that the size distribution, i.e., the nucleation and growth processes, is sensitive to the type of oven.

Bismuth Clusters

Average cluster sizes in the range $D \approx 60-95 \text{ \AA}$ have been studied. The results are given in Table 4 and Fig. 7. The lattice parameters for this range of sizes are essentially constant within an estimated error of 0.3% (note the expanded ordinate in Fig. 7 relative to those in Fig. 5 and Fig. 6). The apparent decrease in c/a ratio with decreasing cluster size is merely suggestive. By comparison with the results for indium and lead, such a change, if any, would be expected to occur below $D \leq 50 \text{ \AA}$. The cluster temperature T_{cl} to be $166 \pm 20^\circ\text{K}$, by the use of extrapolated values for lattice parameter a of 4.54 \AA and for c of 11.83 \AA and bulk thermal expansion coefficients²⁷: $\alpha_a = 11.8 \times 10^{-6} (\text{^\circ C})^{-1}$ ($193 \leq T \leq 373^\circ\text{K}$) and $\alpha_c = 17.7 \times 10^{-6} (\text{^\circ C})^{-1}$ ($150 \leq T \leq 540^\circ\text{K}$). When we use the c/a ratio of 2.606 for the estimation of T_{cl} , it gives a relatively low value of 80°K , while the unit cell volume extrapolation (211.17 \AA^3) provides $T_{cl} = 176^\circ\text{K}$. A simple average of the above is 141°K .

DISCUSSIONS AND CONCLUSIONS

The grain size dependence of the lattice parameters for In, Pb and Bi microclusters has been studied in the range of $40 \leq D \leq 95 \text{ \AA}$. Above $D \geq 60 \text{ \AA}$, the lattice parameters are nearly constant and approach those of the bulk crystalline materials. In the vicinity of $D \approx 50 \text{ \AA}$ (2000 ~ 3000 atoms per cluster), the lattice parameters begin to deviate from those of the larger size clusters. A striking example is the case of In, where a transition from tetragonal to cubic has been observed.

Cluster temperatures, obtained from the lattice parameter extrapolation in the previous section, are 307°K (In), 181°K (Pb) and 141°K (Bi), respectively. It is interesting to compare these values with those estimated from gasdynamic considerations, where it is assumed that the free jet expansion is isentropic and that the cluster temperature is equal to the carrier gas terminal temperature. Recall that the free jets in this work reach their terminal state at $x_T/D_{n2} \approx 1$, that is, only one nozzle diameter downstream. From that point on the flow is essentially collisionless and the gas and cluster temperatures can no longer change except possibly via radiation. Upon computing typical mass flow rates for the metals and for the argon, and using their respective solid and gaseous heat capacities, it is found that the argon in this two phase flow has more than 50 times the heat capacity of the metal microcrystals. Thus computing the argon terminal temperature T_T , using the isentropic equations, involves a negligible error due to the heat exchange between the cluster and the argon carrier gas.

For the largest clusters, such an adiabatic cooling has been calculated and is listed in Table 5: $161\text{-}229^{\circ}\text{K}$ for In, 117°K for Pb and $146\text{-}150^{\circ}\text{K}$ for Bi, respectively. Comparing these to the cluster temperatures listed above, it is possible to examine the temperature lag between the clusters and the expanding argon at the position in the free jet where the electron beam is located, $x_{eb}/D_{n2} \approx 1.5$. Recall that this location is downstream of the position for the terminal Mach number so that the diffraction experiment is sampling a collisionless two phase flow. Figure 8 presents the temperature difference $\Delta T = T_{cl} - T_T$ as a function of cluster temperature for the expansions that contain the larger microclusters (i.e. those approaching the bulk structure). It is seen that ΔT increases as the temperature of the

clusters, and thus also the cluster stagnation temperature prior to expansion, increases. The clusters that start out hotter end up lagging the final argon temperature by a greater amount.

For the clustering of pure gas expansions in free jet molecular beams it has been reported³⁰ that the cluster temperature is linearly proportional to the well depth of inter-atomic (or molecular) potentials. Note in Fig. 8 that the cluster temperature increases from Bi to Pb to In. So also do their heats of sublimation. Thus the observed temperatures of metal clusters correlate almost linearly with the binding energy (i.e. heat of sublimation). Due to the nature of the cluster nucleation and growth process in this work the correlation of cluster temperature involves a somewhat indirect connection with the heat of sublimation. Although the relationship is not direct the correlation is provocative.

In conclusion, the present nozzle assembly for generating metal micro-clusters is suitable for electron diffraction studies of metal cluster structures. Its compactness, ease of handling without the need of a cooling system, and attainment of high temperatures with low electric power, have a good deal of practical merit. In addition, a predictable method for controlling the cluster size distribution has been found. This holds promise for the study of much smaller cluster sizes.

ACKNOWLEDGMENTS

The authors would like to thank Dr. B. G. DeBoer for his helpful discussions with regard to the crystal structures and Messrs. R. Klaub and M. Luczak for their excellent machine work in fabricating the oven source. The financial support for this work from the Power Branch of the Office of Naval Research and the Division of Engineering of the National Science Foundation is gratefully acknowledged.

REFERENCES

1. Ch. Cassagnol, J. de Physique, Phys. Applique, 24, 6A (1963); J de Physique, Phys. Applique, 24, 109A (1963)
2. P. G. Hill, H. Witting, and E. P. Demetri, J. Heat Transfer 85, 303 (1963); G. E. Merritt and R. C. Weatherston, AIAA Journal 6, 721 (1967)
3. M. Volmer, "Kinetic der Phasenbildung," Steinkopf, Dresden (1939) translation ATI No. 81935 from National Technical Information Service
4. A. H. Pfund, Phys. Rev. 35, 1434 (1930); Rev. Sci. Instrum. 1, 397 (1930)
5. C. G. Granqvist and R. A. Buhrman, J. Appl. Phys. 47, 2200 (1976)
6. R. P. Omberg and D. R. Olander, Phys. Fluids 14, 1605 (1971)
7. E. T. Turkdogan, Trans. Am. Inst. Min. Engrs. 230, 740 (1964)
8. M. Epstein and D. E. Rosner, Int. J. Heat Mass Transfer 13, 1393 (1970)
9. J. P. Franck and H. G. Hertz, Z. Physik 143, 559 (1956)
10. J. L. Katz and B. J. Ostermier, J. Chem. Phys. 47, 478 (1967)
11. S. Yatsuga, S. Kasukabe, and R. Uyeda, J. Cryst. Growth 24/25, 319 (1974); S. Kasukabe, S. Yatsuga, and R. Uyeda, Japan. J. Appl. Phys. 13, 1714 (1974)
12. K. Sakurai, S. E. Johnson, and H. P. Broida, J. Chem. Phys. 52, 1625 (1970); D. M. Mann and H. P. Broida, J. Appl. Phys. 44, 4950 (1973); F. Tulfo and D. E. Rosner, Private Communication (1976)
13. H. J. Freund and S. H. Bauer, J. Phys. Chem., 81, 994 (1977); S. H. Bauer and D. J. Frurip, *ibid.* 81, 1015 (1977); D. J. Frurip and S. H. Bauer, *ibid.* 81, 1001; 1007 (1977)
14. S. Yatsuga, S. Kasukabe, and R. Uyeda, Japan. J. Appl. Phys. 12, 1675 (1973)
15. N. Wada, Japan. J. Appl. Phys. 6, 553 (1967); Japan. J. Appl. Phys. 7, 1287 (1968)
16. J. B. Anderson and J. B. Fenn, Phys. Fluids 8, 780 (1965); J. B. Fenn, S. B. Ryali, and M. P. Sinha, "Free Jet Experiments in a Spacecraft Environment," Report from Relay Development Corporation, Branford, Conn. 06405 (1977)
17. G. D. Stein and P. P. Wegener, J. Chem. Phys. 46, 3658 (1967)
18. P. P. Wegener and G. D. Stein, Twelfth Symposium (International) on Combustion, 1183 (1969).
19. M. von Smoluchowski, Phys. Z. 17, 557 (1916); 17, 585 (1916); Z. Phys. Chem. 92, 129 (1917)
20. J. R. Brock and G. M. Hidy, J. Appl. Phys. 36, 1857 (1965)
21. S. C. Graham and J. B. Homer, "Recent Developments in Shock Tube Research," D. Bershader and W. Griffith, Eds., Stanford University Press (1973)

22. J. F. Smith and V. L. Schneider, *J. Less-Common Metals* 7, 17 (1964).
23. J. J. Burton, *Cat. Rev. Sci. Eng.* 9, 209 (1974).
24. P. F. Vergand, *Phil. Mag.* 31, 537 (1975).
25. R. W. Vaughan and H. G. Drickamer, *J. Phys. Chem. Solids* 26, 1549 (1965).
26. *Handbook of Chemistry and Physics*, 43rd ed., page 2278, CRC Press, Ohio (1962).
27. E. F. Cave and L. V. Holroyd, *J. Appl. Phys.* 31, 1357 (1960).
28. H. E. Swanson and E. Tager, *NBS Circular* 539, 1, 34 (1953).
29. P. Cucka and C. S. Barrett, *Acta Cryst.* 15, 865 (1962).
30. G. Torchet, H. Bouchier, J. Farges, M. F. de Feraudy, and B. Raoult, *Proceedings of the Sixth International Symposium on Molecular Beams*, April 18-22, Noordwijkerhooft, Netherlands, B1 (1977).

FIGURE CAPTIONS

- Fig. 1. Schematic diagram of a metal cluster generator for electron diffraction: TC - thermocouple, W - prism mirror window, H - heater for metal vaporization, S_1 and S_2 - sets of screws for configuration adjustments, Ar - argon carrier gas, N_1 and N_2 - flow orifices or nozzles; see text for details.
- Fig. 2. a) The average cluster size D , and b) the cluster production rate \dot{N}_{cl} and the cluster concentration at the crossed beam-intersection N_{cl} are plotted as a function of $p_o T_{om}$, the product of argon stagnation pressure and the temperature at the surface of the evaporating metal. The general trend is that as $p_o T_{om}$ is increased clusters of larger diameter and lower concentration are formed.
- Fig. 3. The microdensitometer traces of electron diffraction photographs for indium and lead microclusters show tetragonal In of an average cluster size of $\sim 63 \text{ \AA}$ in diameter and is compared with cubic (f.c.c) In of $D \approx 45 \text{ \AA}$. A typical f.c.c. pattern of lead is shown with an average size of $\sim 45 \text{ \AA}$. The abscissa S is the scattering parameter $S = (4\pi/\lambda)\sin \theta$ with θ the Bragg angle.
- Fig. 4. A typical diffraction pattern of bismuth clusters with an average cluster size of $\sim 60 \text{ \AA}$ in diameter is plotted as a function of S . The relative intensity here is not calibrated from the photographic density. A rhombohedral Bi structure is assigned by the corresponding hexagonal cell. Some of the Miller indices have been omitted here due to space limitation.

Fig. 5. Lattice parameters and their ratio for the indium microclusters are plotted as a function of the number of atoms per cluster (n) and the average cluster diameter D . Broken lines indicate the corresponding values in bulk crystalline materials at various temperatures. Typical experimental error bars are shown by vertical lines. Deviation from bulk structure begins as the diameter approaches 60 \AA .

Fig. 6. Lattice parameters of lead microclusters are shown with open circles for data from the crucible oven and closed circles for data taken with the coiled tungsten wire oven.

Fig. 7. Lattice parameter ratios of bismuth microclusters are presented as a function of n and D .

Fig. 8. Typical cluster temperatures at the crossed-beam location, as determined from (Debye-Waller factors) and from unit cell parameters are plotted as a function of the difference in temperature between the clusters and the argon carrier gas,

$$\Delta T = T_{cl} - T_T.$$

Table I

OVEN OPERATING CHARACTERISTICS

Dimensions

heater - argon supply jet	= 0.6 cm	argon supply jet diameter, d_a	= 0.096 cm
heater - thermocouple	= 0.93 cm	nozzle N_1 diameter, dN_1	= 0.075 cm
heater - nozzle N_1	= 1.3 to 2.6 cm	nozzle N_2 diameter, dN_2	= 0.05 cm
$N_1 - N_2$	= 0.3 cm		
N_2 - electron beam	= 0.075 ± .025 cm		

Typical Oven Properties
(Range of properties in parenthesis)

Location	Pressure Torr	Temperature °K	Argon		Mean Free Path cm	Knudsen No.-Kn	Velocity cm/sec	Reynolds No.-Re	Mach No.-M	Flow Time sec
			Mass Flow Rate g/sec	Rate						
exit of argon supply jet	1.0 (0.5-1.2)	300	.033	.033	5.0×10^{-3}	0.050	15,000	20	0	0.2 (0.015-0.4)
entrance to nozzle N_1	1.0 (0.5-1.2)	400 (340-650)	.033	.033	6.6×10^{-3}	0.088	~30,000	18	~0.01	10×10^{-6}
entrance to nozzle N_2	0.6 (0.3-0.7)	315 (268-512)	.0265	.0265	1.1×10^{-2}	0.214	27,000 [†]	9.5	0.9	2×10^{-6}
at electron beam	1×10^{-5} ^{**} (1×10^{-5} - 1.4×10^{-5})	117 (100-190)	.0265	.0265	500 ^{**}	>>1	46,800	-	2.5*	

* This is the terminal Mach No. in the free jet¹⁶ and occurs at $x/D_{n_2} \approx 1$ or 0.05 cm from nozzle N_2 .

** These values are for the background gas.

† This is an upper limit, it could be as much as an order of magnitude lower.

TABLE 2
INDIUM CLUSTER RESULTS

In	D(\AA) ^{a)}	c(\AA) ^{b)}	a(\AA) ^{b)}	c/a	p _o (torr) ^{c)}	T _o ($^{\circ}$ K) ^{d)}	T _{om} ($^{\circ}$ K) ^{e)}	Exposure time (sec) ^{f)}
1	81	4.903	4.642	1.056	0.91	568	1344	2
2	81	4.880	4.606	1.059	0.91	450	1205	10
3	68	4.891	4.627	1.057	0.91	460	1205	7
4	63	4.874	4.644	1.048	0.91	568	1344	5
5	63	4.871	4.617	1.055	0.50	420	1310	10
6	62	4.848	4.608	1.052	0.75	440	1310	10
7	52	4.751	4.663	1.019	0.67	395	1144	30
8	51	4.712	4.712	1.00	0.67	376	1144	25
9	50	4.707	4.707	1.00	0.71	420	1158	20
10	44	4.731	4.731	1.00	0.63	410	1144	45
11	44	4.704	4.704	1.00	0.71	410	1144	40
12	42	4.712	4.712	1.00	0.71	445	1158	30
Bulk ^{g)}	∞	4.945	4.600	1.075	at 298 $^{\circ}$ K			

- a) average cluster diameter; estimated error range of 5-15 \AA .
- b) lattice parameters for face-centered tetragonal and face-centered cubic structures; the experimental errors are estimated to be 0.3-0.4%.
- c) argon carrier gas pressure in the mixing region; see text.
- d) ambient temperature at the mixing region, measured by a Alumel-Chromel thermocouple; see Fig. 1.
- e) tungsten wire temperature measured by an optical pyrometer.
- f) exposure time of electron diffraction photographs, beam current ca. 4.6 μA .
- g) bulk crystalline material data, taken from Ref. 22.

TABLE 3
LEAD CLUSTER RESULTS^{a)}

Pb	D(Å)	a(Å)	p _o (torr)	T _o (°K)	T _{om} (°K)	Exposure time(sec)
1	82	4.939	0.83	352	1266	30
2	60	4.938	0.67	423	1333	20
3	51	4.939	0.50	410	1205	30
4	40	4.935	0.55	376	1205	20
5*	51	4.933	1.0	640	1283	20
6*	51	4.929	0.98	616	1166	20
7*	49	4.937	0.98	688	1339	23
8*	44	4.937	1.08	688	1286	30
9*	40	4.932	1.0	640	1283	15
Bulk ^{b)}	∞	4.9505	at 298°K			

a) see the footnotes of Table 2. The plate numbers with * correspond to data taken by the use of a boron nitride oven, while for the rest of the plates a tungsten wire oven was used; see text.

b) bulk crystal, taken from Ref. 28.

TABLE 4
BISMUTH CLUSTER RESULTS^{a)}

Bi	D(Å)	a(Å)	c(Å)	c/a	p _o (torr)	T _c (°K)	T _{om} (°K)	Exposure time(sec)
1	94	4.54	11.83	2.606	0.83	415	-	20
2	78	4.54	11.83	2.606	0.53	352	1366	40
3	60	4.55	11.81	2.594	0.55	340	1177	20
Bulk ^{b)}	∞	4.546	11.862	2.609	at 298°K			

a) see the footnotes of Table 2. The lattice parameters a and c are those for a hexagonal cell.

b) bulk crystal data taken from Ref. 29.

TABLE 5

ESTIMATION OF CLUSTER TEMPERATURE FROM GASDYNAMICS

Sample	p_o (torr) ^{a)}	T_o (°K) ^{b)}	M_T ^{c)}	T_T (°K) ^{d)}
In-1	0.91	568	2.11	229
In-2	0.91	450	2.32	161
Pb-1	0.83	352	2.46	117
Bi-1	0.83	415	2.31	150
Bi-2	0.53	352	2.06	146

a) argon pressure inside the nozzle.

b) ambient temperature in the mixing region; see Figure 1.

c) terminal Mach number: cf Table 1.

d) terminal gas temperature which is a lower limit for the cluster temperature, i.e. for a finite heat transfer rate from cluster to the cooling gas the cluster temperature is greater than the terminal gas temperature,
 $T_{cl} > T_T$.

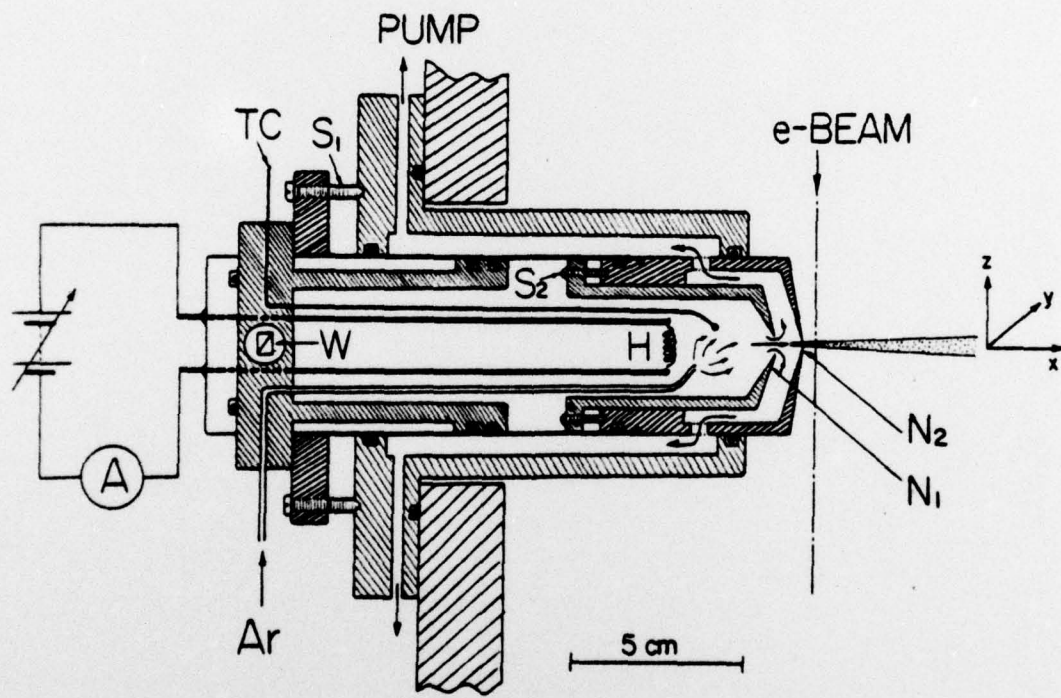


Figure 1

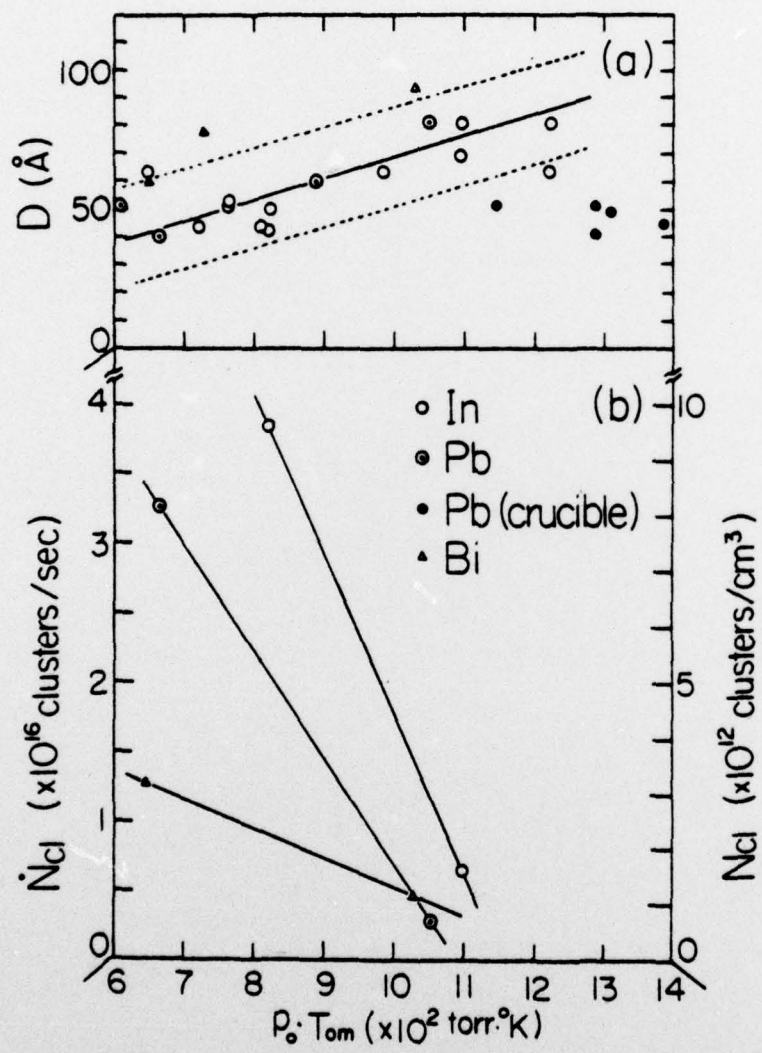


Figure 2

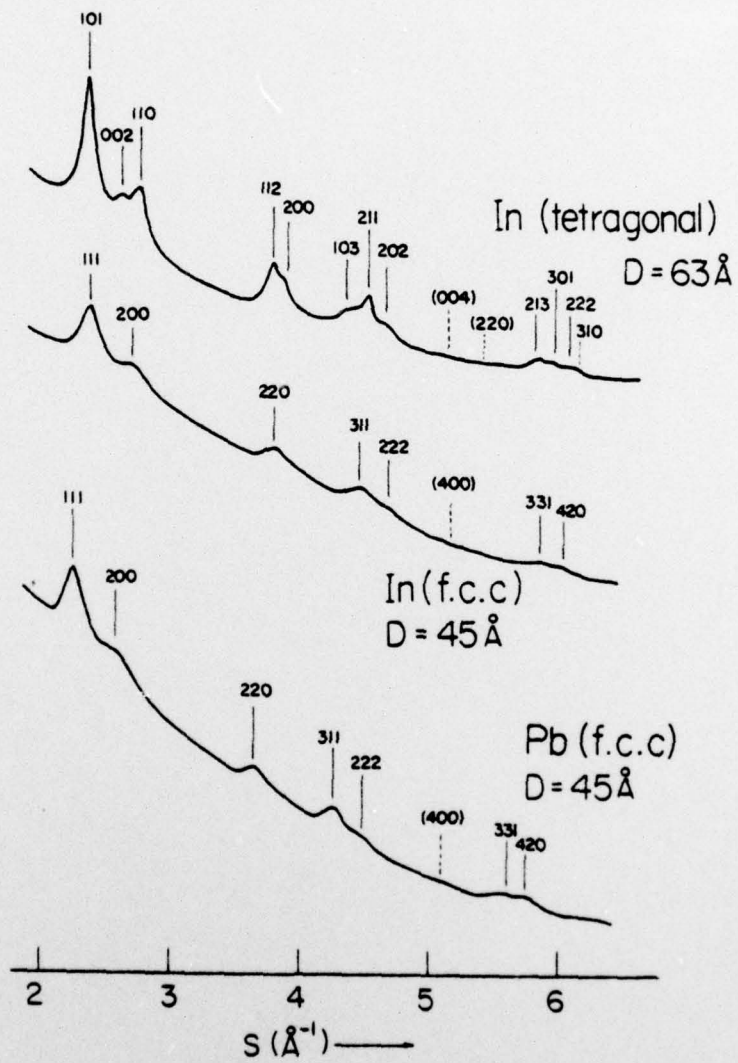


Figure 3

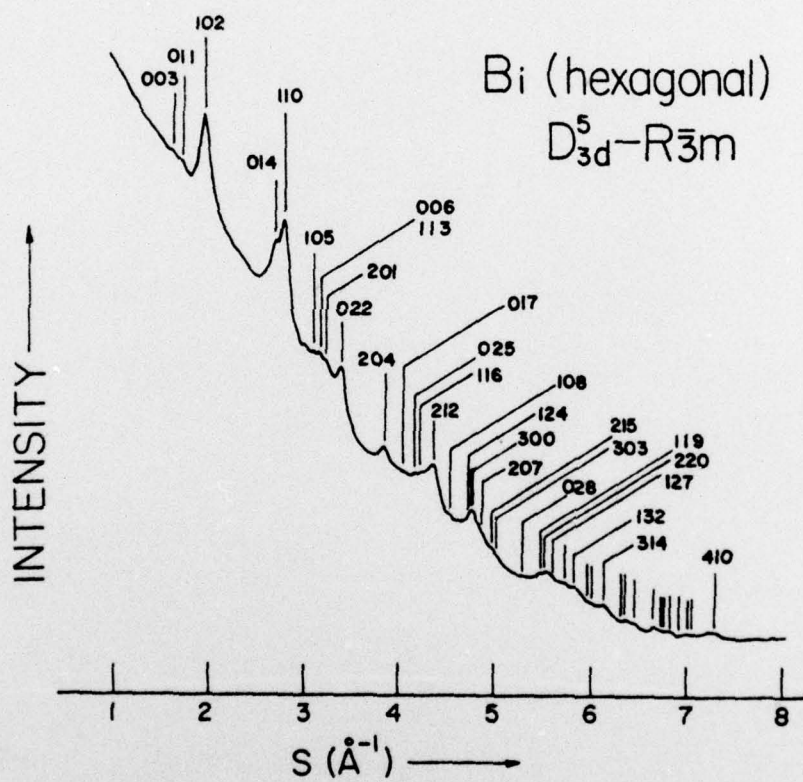


Figure 4

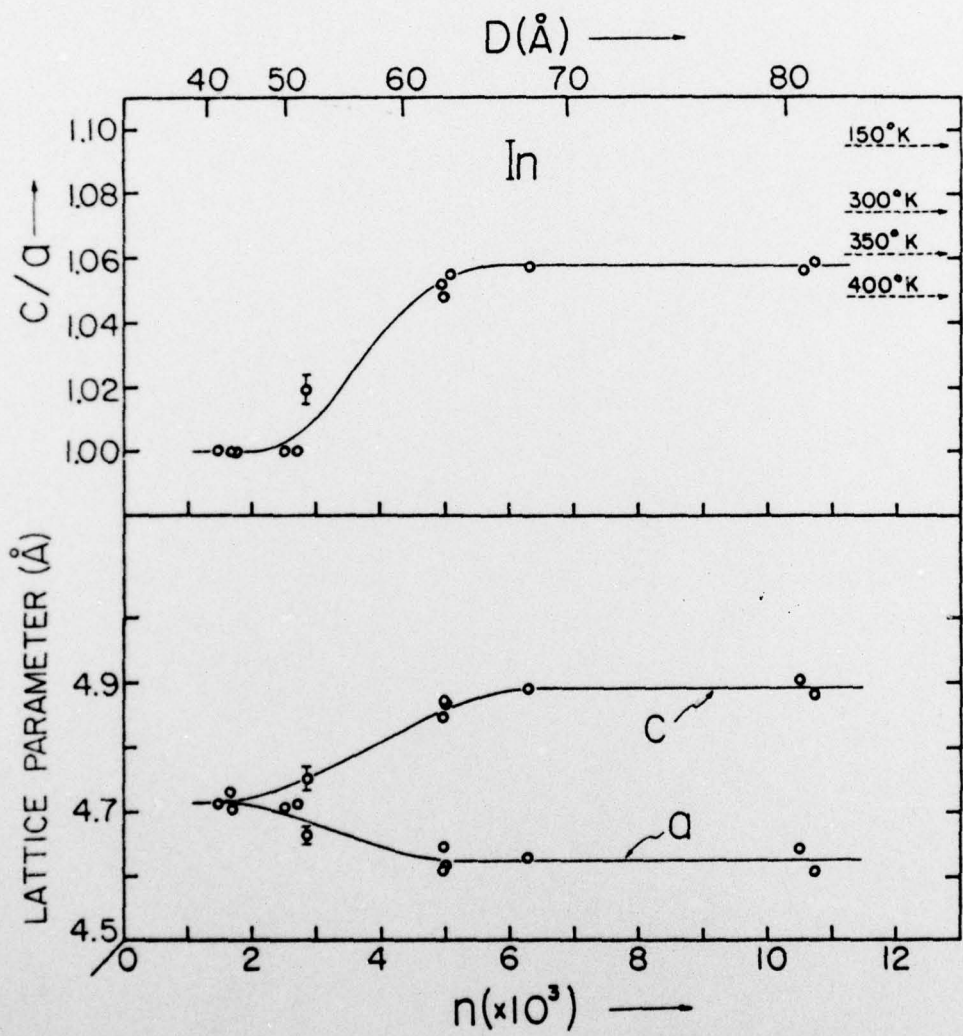


Figure 5

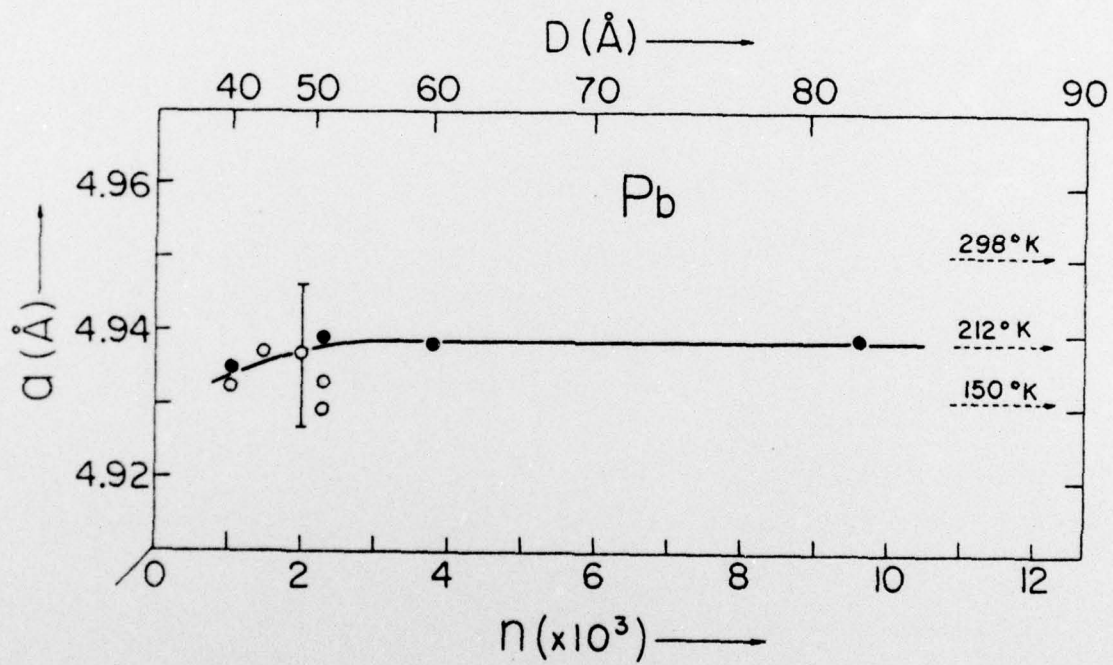


Figure 6

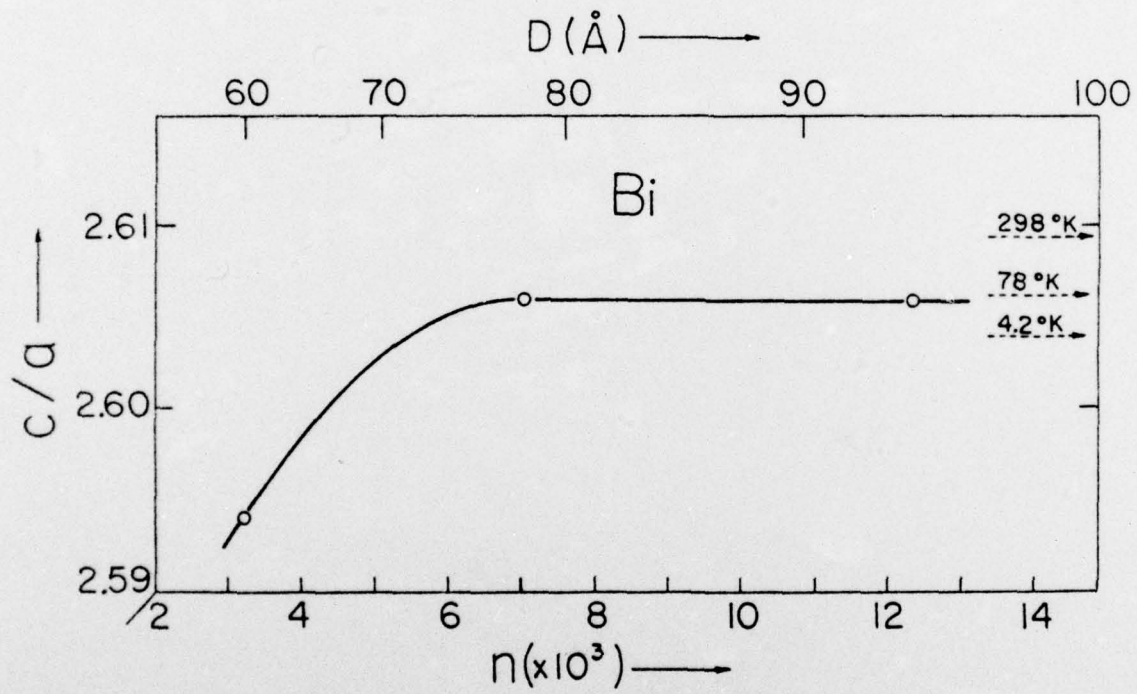


Figure 7

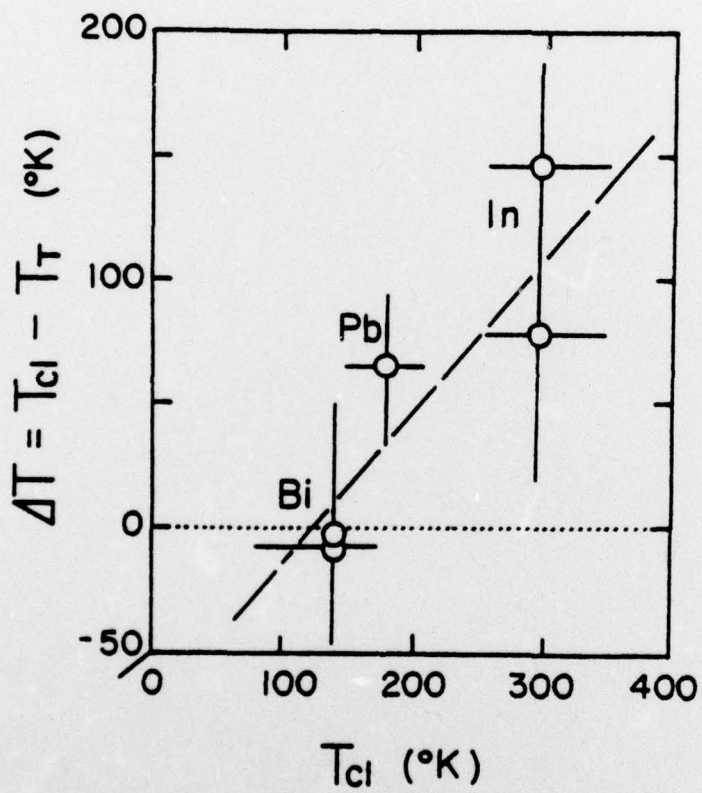


Figure 8